ELSEVIER

Effect of Zn^{2+}-Sn^{4+} co-substitution on structural and magnetic properties of $SrFe_{12-2x}Zn_xSn_xO_{19}$ ($x = 0–2$) M-type strontium ferrite

Xiang Yu [a,b], Ningfang Zhou [b], Ruoshui Liu [a,b,d], Lichen Wang [b,c], Zhiyi Xu [a,b], Huayang Gong [b], Tongyun Zhao [a,b], Jirong Sun [a], Fengxia Hu [a], Baogen Shen [a,b,c,d,*]

[a] Beijing National Laboratory for Condensed Matter Physics, Institute of Physics, Chinese Academy of Sciences, Beijing, 100190, China
[b] Ganjiang Innovation Academy, Chinese Academy of Sciences, Ganzhou, Jiangxi, 341119, China
[c] Ningbo Institute of Materials Technology & Engineering, Chinese Academy of Sciences, Ningbo, Zhejiang, 315201, China
[d] School of Rare Earths, University of Science and Technology of China, Hefei, Anhui, 230026, China

ABSTRACT

We studied the structure and magnetic properties of Zn^{2+}-Sn^{4+} co-substituted M-type strontium ferrite by X-ray diffraction (XRD), Fourier transformer infrared (FT-IR) spectroscopy, Raman spectroscopy, scanning electron microscopy (SEM), and superconducting quantum interference device magnetometer (SQUID-VSM). The lattice constants a and c increase monotonically with increasing substitution x, which is primarily attributed to the fact that the ionic radii of Zn^{2+} and Sn^{4+} are larger than those of Fe^{3+}. The room temperature magnetic measurement results indicate that the saturation magnetization (M_s) can reach the maximum value $M_s = 77$ emu/g when $x = 0.25$, originating from the occupation of Zn^{2+} and Sn^{4+} in the spin-down $4f_1$ and $4f_2$ sites, respectively. Next, when $x \geq 0.5$, the nonmagnetic Zn^{2+} and Sn^{4+} weaken the superexchange interaction, resulting in a monotonic decrease in saturation magnetization and coercivity. The sample with $x = 0.25$ has the optimum magnetic properties of $M_s = 77$ emu/g, $M_r = 35$ emu/g and $H_c = 2203$ Oe, and it is a promising candidate for high-density magnetic recording materials.

1. Introduction

M-type hexagonal ferrite ($BaFe_{12}O_{19}$, BaM or $SrFe_{12}O_{19}$, SrM) has a widespread use in the fields of permanent magnet [1–3], high-density magnetic recording [4–6], microwave absorption [7–12] and ferroelectric materials [13–15] because of its high magnetocrystalline anisotropy, modest saturation magnetization (M_s) and relatively low manufacturing cost, etc [16,17]. As a typical magnetic material, M-type hexagonal ferrite can be prepared by the conventional ceramic route [18], sol-gel method [19], and hydrothermal method [20]. Among them, the conventional ceramic route is a generally utilized way in industrial production with the advantage of low cost, yet the particles have a wide size distribution simultaneously. Hence, the demand for high-performance M-type hexagonal ferrite is increasing along with the continuous development of modern science and technology. In the past decades, researchers have been committed to improving the magnetic properties of M-type hexagonal ferrite in various ways. For instance, improving the grain size distribution of M-type hexagonal ferrite by adding auxiliary agents [21,22], optimizing the magnetic properties of

M-type hexagonal ferrite through soft/hard magnetic exchange coupling [23,24], and sintering high-performance M-type hexagonal ferrite using nanoparticles as iron source [25,26], etc. As one of the effective means to adjust the magnetic properties of M-type hexagonal ferrite, ion substitution has been widely adopted by researchers, such as Sm^{3+} [27], Eu^{3+} [28] and Gd^{3+} [29] substitute for Sr^{2+}, La^{3+}-Co^{2+} [30], Ce^{3+}-Mn^{2+} [31] and Pr^{3+}-Zn^{2+} [32] substitute for Sr^{2+}-Fe^{3+}, and Al^{3+} [10], In^{3+} [15], Ga^{3+} [33], Ti^{4+} [11], Co^{2+}-Ti^{4+} [34], Cd^{2+}-Zr^{4+} [35] and Zn^{2+}-Ir^{4+} [36] substitute for Fe^{3+}. Although researchers have achieved beneficial results through the above-mentioned ion substitution methods, it is still necessary to find new ion substitution strategies to meet the needs of M-type hexagonal ferrite applications.

The crystal structure of BaM or SrM is hexagonal structure and the space group is $P6_3/mmc$. O^{2-} and Ba^{2+} or Sr^{2+} form a close-packed arrangement and Fe^{3+} located in these interstitial sites. There are five Fe sites in the structure of M-type hexagonal ferrite, $2a$, $12k$, and $4f_2$ are octahedral sites, $4f_1$ is tetrahedral site, and $2b$ is bipyramidal site. Owing to orbital quenching, the magnetic moment of Fe^{3+} is only derive from the spin magnetic moment. Among these five sites, the spin direction of


Fe^{3+} is upward in $2a$, $2b$ and $12k$ sites, and the spin direction of Fe^{3+} is downward in $4f_1$ and $4f_2$ sites. There are 24 Fe^{3+} in a M-type hexagonal ferrite unit cell, of which 16 Fe^{3+} occupy $2a$, $2b$ and $12k$ sites (spin-up) and the other 8 Fe^{3+} occupy $4f_1$ and $4f_2$ sites (spin-down). Since the magnetic structure of M-type hexagonal ferrite described by the Néel theory of antiferromagnetism, the net magnetic moment of M-type hexagonal ferrite is 40 μ_B in a unit cell (i.e. the sum of the magnetic moments of 8 Fe^{3+} at spin-up sites) [17,37–39]. As the magnetic properties of M-type hexagonal ferrite are essentially originated from Fe^{3+} in five different crystalline sites, ion substitution will change the microscopic magnetic structure and consequently affect the macroscopic magnetic properties [18,33,40–42]. In this regard, the substitution of non-magnetic ions into Fe sites with spin-down has the potential to be an effective way to enhance the M_s of M-type hexagonal ferrite. Based on this idea, researchers have successfully improved the M_s of M-type hexagonal ferrite through La^{3+}-Zn^{2+} co-substitution [43], Nd^{3+}-Zn^{2+} co-substitution [44] and Cd^{2+}-Zr^{4+} co-substitution [35], etc.

In recent years, some researchers have found that Zn^{2+}-Sn^{4+} co-substitution is expected to become one of the effective ways to optimize the M_s of SrM. Liyanage et al. studied the ion occupancy and magnetic properties of $SrFe_{11}Zn_{0.5}Sn_{0.5}O_{19}$ through the first principles total-energy calculations. They found that Zn^{2+} and Sn^{4+} tend to occupy the $4f_1$ and $4f_2$ sites with the lowest energy configuration, respectively. In terms of magnetic properties, Zn^{2+}-Sn^{4+} co-substitution will significantly raise the M_s of SrM and reduce its magnetic anisotropy [38]. Dixit et al. have also carried out detailed research on Zn^{2+} and Sn^{4+} substituted SrM using first principles and density functional theory. They found that the M_s and magnetocrystalline anisotropy of SrM were closely related to the five Fe sites. The calculation results present that the possibility of Zn^{2+} occupying $4f_1$ site can reach 78% in $SrFe_{11.5}Zn_{0.5}O_{19}$, while Sn^{4+} will occupy $12k$ and $4f_2$ sites with approximately the identical probability in $SrFe_{11.5}Sn_{0.5}O_{19}$. When Zn^{2+}-Sn^{4+} co-substitution is used, Zn^{2+} and Sn^{4+} will occupy $4f_1$ and $4f_2$ sites with a high probability of 82% in $SrFe_{11}Zn_{0.5}Sn_{0.5}O_{19}$. Zn^{2+} and Sn^{4+} simultaneously occupy the spin-down sites, the M_s of the material will be dramatically improved [39]. Herein, we synthesized $SrFe_{12-2x}Zn_xSn_xO_{19}$ ($x = 0$, 0.25, 0.5, 1, 1.5, 2) samples through the conventional ceramic route. Zn^{2+}-Sn^{4+} co-substitution can effectively improve the M_s and reduce the H_c of SrM, and the material is expected to be a candidate for high-density magnetic recording materials.

2. Experimental

2.1. Materials and synthesis

$SrFe_{12-2x}Zn_xSn_xO_{19}$ ($x = 0$, 0.25, 0.5, 1, 1.5, 2) samples were prepared via conventional ceramic method. The raw materials required for samples preparation are Fe_2O_3 (Aladdin, 99.9%), $SrCO_3$ (Aladdin, 99.95%), SnO_2 (Aladdin, 99.9%) and ZnO (Aladdin, 99.9%). The raw materials were fully mixed by planetary ball mill (Nanjing Boyuntong Instrument, XGB4) for 3 h. Agate balls with three sizes (diameter of 20 mm, 10 mm and 6 mm) were placed in the agate ball milling tank. The ball to powder ratio was selected as 20:1. In all the samples, the (Fe/Zn/Sn)/Sr atomic ratio is 12:1. After that, the mixtures were dried and sintered at 1250 °C for 40 min. Finally, the prepared samples were cooled to room temperature for further physical property measurement. The entire reaction process is described by the following formula:

$$(6-x)\ Fe_2O_3 + SrCO_3 + x\ ZnO + x\ SnO_2 \rightarrow CO_2 \uparrow + SrFe_{12-2x}Zn_xSn_xO_{19}$$
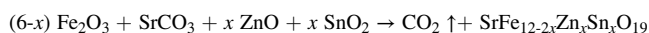
2.2. Characterizations

X-ray diffractometer (XRD, BRUKER D8 ADVANCE) with Cu K_α radiation ($\lambda = 1.54184$ Å) was used for phase identification of the samples.

The refinement of XRD data was performed by TOPAS software to obtain the lattice parameters and phase composition. The infrared spectra of the samples were obtained by a Fourier transformer infrared spectrometer (FT-IR, ThermoFisher Nicolet iS 5). Raman spectra was record using a micro-Raman spectroscopy (RENUSHAW inVia Raman Microscope) at room temperature. The size and morphology of the samples were studied by a scanning electron microscope (SEM, TESCAN CLARA). The particle size distribution of the sample was measured with a laser particle analyzer (Sympatec GmbH, HELOS/BR-OM-RODOS). The magnetic hysteresis loops were measured at 300 K by a superconducting quantum interference device magnetometer (SQUID-VSM, Quantum Design) under applied field of ±50,000 Oe.

3. Results and discussion

3.1. X-ray diffraction analysis

XRD patterns of $SrFe_{12-2x}Zn_xSn_xO_{19}$ ($x = 0$, 0.25, 0.5, 1, 1.5, 2) are shown in Fig. 1. The main phases of all the samples show hexagonal crystal structure, which is consistent with the standard card (COD#1008856). A few impurities in the sample with $x = 0$, 0.25 and 2 were detected. The diffraction peaks of the impurities were located at about $2\theta = 33°$, $33°$ and $26°$, which were attributed to Fe_2O_3, Fe_2O_3 and SnO_2, respectively.

As shown in Fig. 2a, the diffraction peaks shift to the left as increasing Zn^{2+}-Sn^{4+} co-substitution. The peak (107) gradually shifted from 32.37° ($x = 0$) to 32.28° ($x = 0.25$), 32.24° ($x = 0.5$), 32.16° ($x = 1$), 32.04° ($x = 1.5$) and 31.85° ($x = 2$). Similarly, the peak (114) shifted from 34.22° ($x = 0$) to 34.14° ($x = 0.25$), 34.10° ($x = 0.5$), 34.03° ($x = 1$), 33.91° ($x = 1.5$) and 33.77° ($x = 2$). According to Bragg's equation (1):
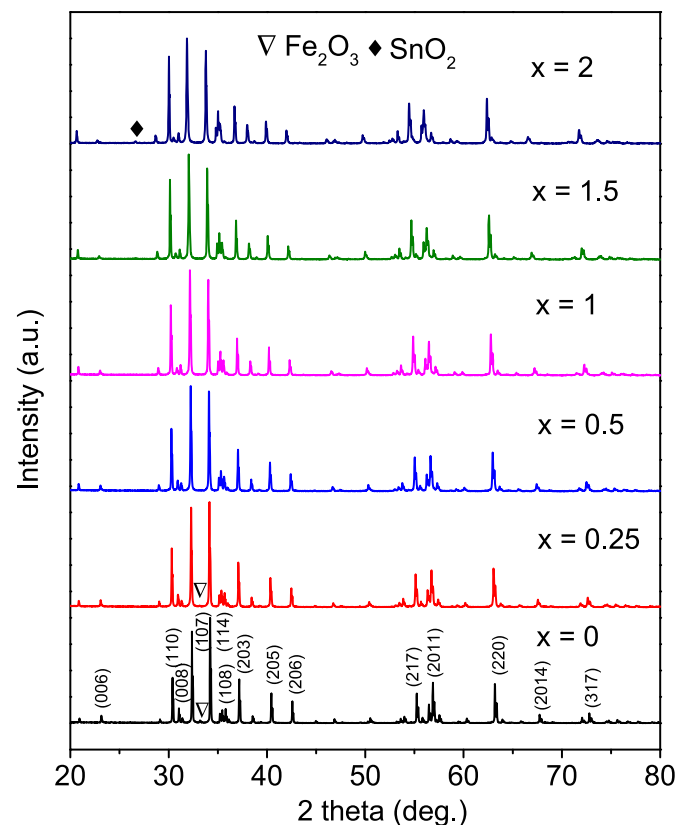
$$2d \sin \theta = n\lambda \tag{1}$$

Fig. 1. X-ray diffraction patterns of the $SrFe_{12-2x}Zn_xSn_xO_{19}$ ($x = 0$, 0.25, 0.5, 1, 1.5, 2).
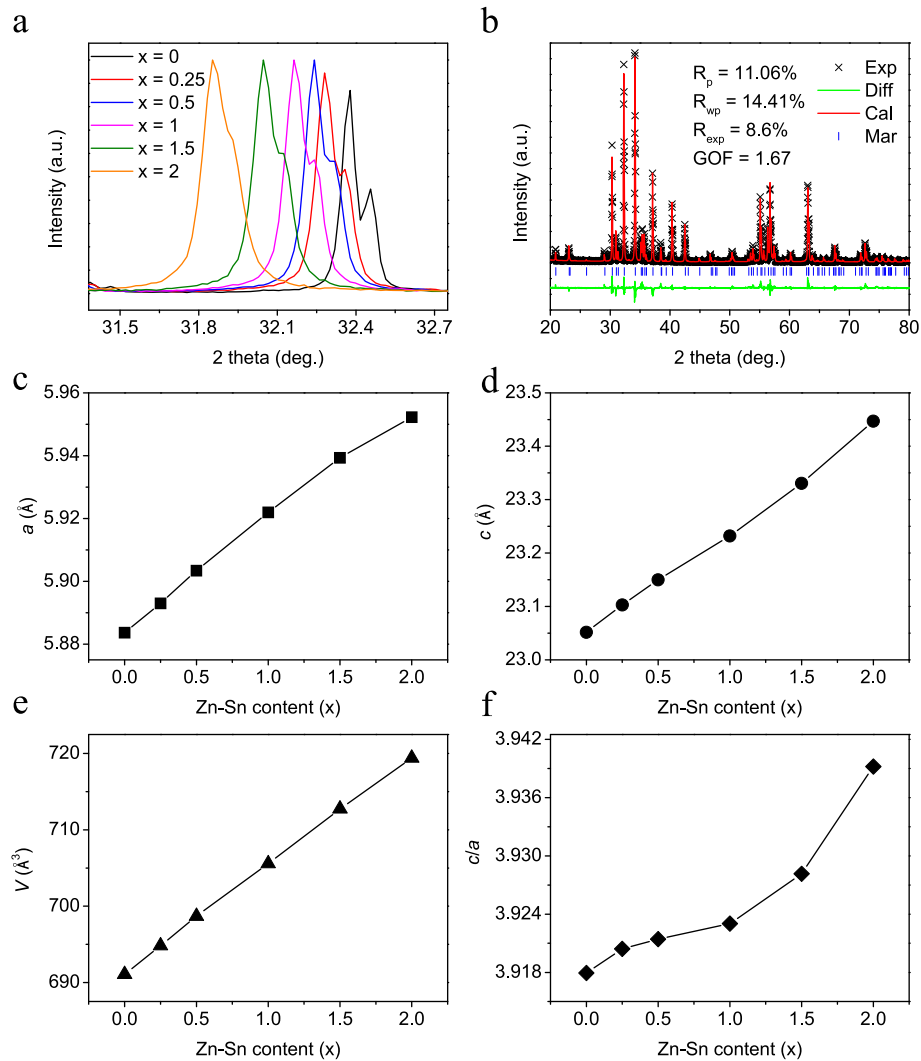
Fig. 2. (a) The enlargement of XRD patterns in the range of 31.5°–32.7°. (b) Refined X-ray diffraction pattern of the sample with x = 0.25. Variations of lattice constants (c) *a*, (d) *c*, (e) cell volume V_{cell} and (f) *c/a* for the $SrFe_{12-2x}Zn_xSn_xO_{19}$ (*x* = 0, 0.25, 0.5, 1, 1.5, 2).

where *d* is the interplanar spacing, *θ* is the angel of diffraction, *n* is the order of diffraction pattern and *λ* is the wavelength of X-rays. Since *n* and *λ* are constants, it can be seen that *θ* will decrease with increasing *d*. Therefore, the results display that Zn^{2+}-Sn^{4+} co-substitution will cause lattice expansion of the sample. In order to achieve more detailed phase composition and structural information, the XRD data was refined by TOPAS software. Fig. 2b shows the refined XRD patterns of a representative sample with *x* = 0.25. The refinement parameter, R_p, R_{wp}, R_{exp} and GOF, was maintained below 15%, 15%, 10% and 2 respectively to ensure data reliability (Table 1). Lattice parameters *a* and *c* and cell volume V_{cell} can be calculated according to equation (2) and equation (3):

$$\frac{1}{d_{hkl}^2} = \frac{4}{3} \cdot \frac{h^2 + hk + k^2}{a^2} + \frac{l^2}{c^2} \tag{2}$$

where d_{hkl} is the interplanar spacing, *h*, *k* and *l* are the Miller indices of the crystal plane corresponding to the diffraction peak, and *a* and *c* are the lattice parameters.

$$V_{cell} = \frac{\sqrt{3}}{2} a^2 c \tag{3}$$

where V_{cell} is the cell volume, *a* and *c* are the lattice parameters. Fig. 2c and d show the lattice parameters *a* and *c* increase monotonically with increasing Zn^{2+}-Sn^{4+} co-substitution, and the corresponding cell volume V_{cell} also increases (Fig. 2e). According to the results of theoretical calculations in the literature [39], Zn^{2+} mainly occupy $4f_1$ site while Sn^{4+} mainly occupy $4f_2$ site. The ionic radii of Fe^{3+} in tetrahedra (FeO_4, the coordination number is 4) and octahedra (FeO_6, the coordination number is 6) is 0.49 Å and 0.55 Å, respectively, while that of Zn^{2+} in the tetrahedron is 0.6 Å and that of Sn^{4+} in the octahedron is 0.69 Å [45]. The substitution of Zn^{2+} and Sn^{4+} with larger ion radius for Fe^{3+} resulted in obvious lattice expansion in SrM. It is known that parameters *c/a* can be used to identify structural types. According to the literature [46], when the parameter *c/a* is lower than 3.98, the structure of ferrite is identified as M-type magnetoplumbite structure. As shown in Fig. 2f,

Table 1
The XRD refinement parameters.

x	R_p	R_{wp}	R_{exp}	GOF
0	14.13	10.38	9.21	1.53
0.25	14.41	11.06	8.6	1.67
0.5	14.665	10.63	8.28	1.77
1	14.809	9.94	7.86	1.88
1.5	14.265	9.57	7.26	1.97
2	13.35	8.59	7	1.91

the parameters c/a of all the samples are lower than 3.98, which indicates that the prepared $SrFe_{12-2x}Zn_xSn_xO_{19}$ ($x = 0$, 0.25, 0.5, 1, 1.5, 2) are M-type magnetoplumbite structure. From the perspective of phase composition, the content of Fe_2O_3 is 1.81% and 0.95% for the sample with $x = 0$ and 0.25, respectively. The sample contains a small amount of Fe_2O_3, which is common in SrM synthesized from the raw materials with Fe/Sr atomic ratio of 12. With increasing Zn^{2+}-Sn^{4+} co-substitution, the content of Fe_2O_3 gradually decreases, and no Fe_2O_3 is found in the samples with higher co-substitution amount. Combined with the results of lattice parameters, this may be because lattice expansion is conducive to ion diffusion, thus eliminating Fe_2O_3 impurities. Furthermore, there are only 0.61% of SnO_2 in the sample with $x = 2$, which suggests that nearly four Fe^{3+} ions can be substituted by Zn^{2+} and Sn^{4+}, that is, Zn^{2+} and Sn^{4+} have relatively high solid solubility in SrM.

3.2. Fourier transformer infrared (FT-IR) spectroscopy analysis

The FT-IR spectra of in the range of 2000–400 cm^{-1} at room temperature plotted in Fig. 3. And the principle of FT-IR spectroscopy is in accordance with the spring-model of atom vibration, the wave number v of the vibration is expressed as follows:

$$v = \frac{1}{2\pi c}\sqrt{\frac{k}{\mu}} \qquad (4)$$

where the wavenumber, speed of light, the spring constant, and the reduced mass of ions are each represented by v, c, k and μ respectively [47]. All the samples show typical absorption bands of M-type hexagonal structure. The characteristic absorption bands at around 600 cm^{-1}, 550 cm^{-1} and 440 cm^{-1} belongs to the stretching vibrations of tetrahedral sites and octahedral sites in hexagonal systems [20]. With increasing Zn^{2+}-Sn^{4+} co-substitution, the band near 600 cm^{-1} shifted monotonically to 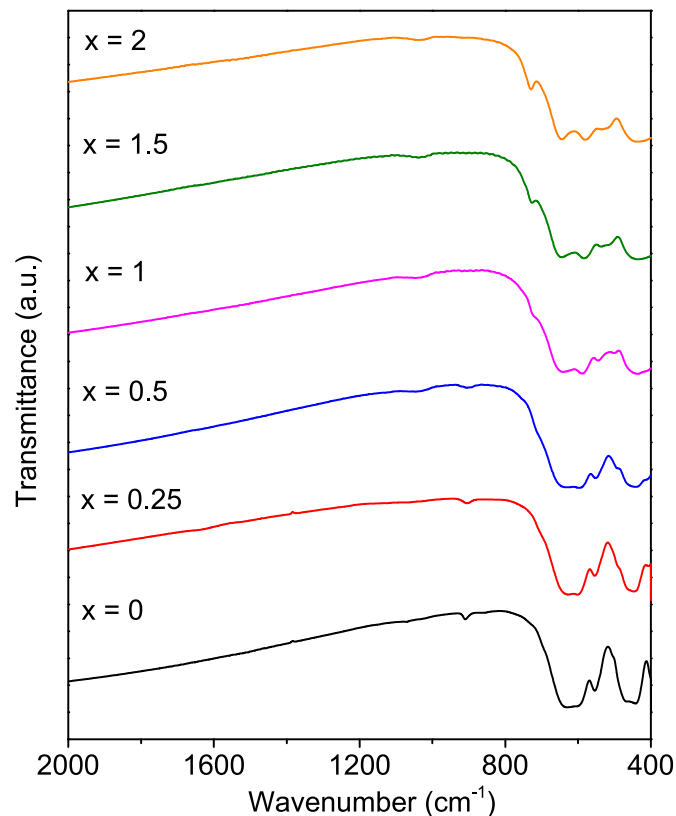lower wave number, which is stemming from the substitution mass effect of Zn^{2+} and Sn^{4+} [34,48,49]. For the samples with $x \geq 1$, a new band appears in the range of 500–550 cm^{-1} corresponds to the Zn–O or Sn–O absorption band reported in the literature [50,51]. The other new bond at 720 cm^{-1} should be attributed to octahedral complexes with the Sn-Fe [51]. Among the samples, the relative intensities of absorption bands are slightly different in the co-substituted samples, which is mainly due to the change of the Fe–O bonds distance [44].

3.3. Raman studies

Raman spectroscopy can be employed to study the dynamic behavior of cations at different sites and cationic distribution in crystal structure. According to group theoretical methods, the 64 ions in the unit cell of hexagonal ferrite give rise to 189 optics modes ($k = 0$), including 42 Raman active modes ($11A_{1g} + 14E_{1g} + 17E_{2g}$) [52]. The Raman spectra of $SrFe_{12-2x}Zn_xSn_xO_{19}$ ($x = 0$, 0.25, 0.5, 1, 1.5, 2) were measured to obtain the information of crystal structure and vibrational modes, as shown in Fig. 4. The sample with $x = 0$ exhibits typical SrM characteristics, and its vibration modes centered at about 277 cm^{-1}, 317 cm^{-1}, 336 cm^{-1}, 403 cm^{-1}, 465 cm^{-1}, 524 cm^{-1}, 615 cm^{-1}, 682 cm^{-1} and 729 cm^{-1}. The strongest mode at 682 cm^{-1} is attributed to the bipyramidal FeO_5 ($2b$ site) with A_{1g} symmetry. The mode at 615 cm^{-1} is dominated by the octahedra FeO_6 ($4f_2$ site) with A_{1g} symmetry, while the mode at 729 cm^{-1} is dominated by motions of the tetrahedral FeO_4 ($4f_1$ site) with A_{1g} symmetry. The mode at 277 cm^{-1} and 524 cm^{-1} are attributed to E_{1g} symmetry, while the mode at 317 cm^{-1} is attributed to E_{2g} symmetry. The mode at 403 cm^{-1} is assigned to the octahedra FeO_6 ($12k$ site) with A_{1g} symmetry. The mode at 465 cm^{-1} and 336 cm^{-1} are belong to mixed octahedra FeO_6, which are associated with the $12k$ site and the $2a$ site [52–54]. In the samples with Zn^{2+}-Sn^{4+} co-substitution, it can be found that there are considerable shifts of Raman characteristic
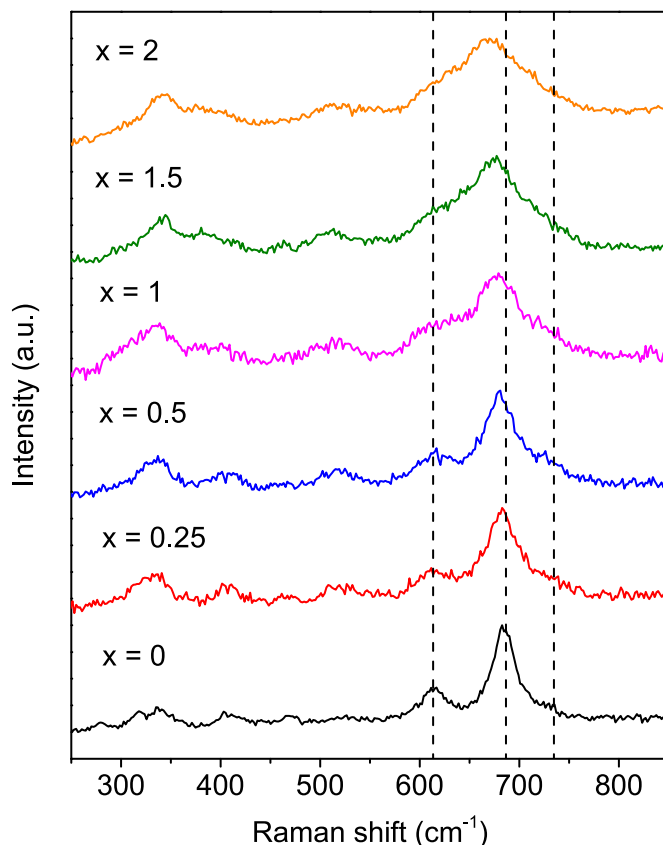

Fig. 3. Fourier transformer infrared spectra of the $SrFe_{12-2x}Zn_xSn_xO_{19}$ ($x = 0$, 0.25, 0.5, 1, 1.5, 2).

Fig. 4. Raman spectra of the $SrFe_{12-2x}Zn_xSn_xO_{19}$ ($x = 0$, 0.25, 0.5, 1, 1.5, 2).

peaks stemming from mass effect and force constant, among which the change of force constant is due to bond length, lattice parameters and ionic valence, etc [55]. For the main peak at 682 cm^{-1} of Raman spectra, the peak shifts to the lower wave number with increasing Zn^{2+}-Sn^{4+} co-substitution. Combined with the results of the refinement of XRD data, the downshift in the wave number should be caused by lattice expansion. It can be found that there is broadening in the mode at 615 cm^{-1} ($4f_2$ site) and 729 cm^{-1} ($4f_1$ site). Referring to the first-principles calculation results in the literature [39], this correlate with the fact that Zn^{2+} and Sn^{4+} with larger ionic radii occupy the $4f_1$ site and the $4f_2$ site, respectively, which is causing local tetrahedral FeO_4 and octahedral FeO_6 distortions. This Raman experimental results can be well matched with the theoretical study results for the occupancy of Zn^{2+} and Sn^{4+}.

3.4. Morphological and size analysis

The scanning electron microscopy (SEM) images of the $SrFe_{12-2x}Zn_xSn_xO_{19}$ (x = 0, 0.25, 0.5, 1, 1.5, 2) are exhibited in Fig. 5a–f, and the sizes of all the samples are about 1–2 μm. The samples (x = 0–2) gradually change from granular to platelets-like, which should be related to Zn^{2+}-Sn^{4+} co-substitution. A similar variation has also been found in Co^{2+}-Ti^{4+} co-substituted barium hexaferrite, which is mainly due to the change of the activation energy of nucleation by Co^{2+}-Ti^{4+} co-substitution [56]. Additionally, the particle sizes of samples were also measured by laser particle analyzer, and all samples showed two peaks

on the size distribution diagram (Fig. 5g). The peaks near 30 μm are caused by agglomeration between particles during high-temperature sintering. The other peaks near 2 μm are close to the size exhibited in SEM.

3.5. Magnetic studies

Fig. 6a shows the magnetic hysteresis loops of $SrFe_{12-2x}Zn_xSn_xO_{19}$ (x = 0, 0.25, 0.5, 1, 1.5, 2) at 300 K. It can be seen that different samples have different dependence on magnetic field. With increasing Zn^{2+}-Sn^{4+} co-substitution, the M_s of samples shows a trend of increasing first and then decreasing (Fig. 6b). According to the literature, the change of M_s can be explained by Zn^{2+} and Sn^{4+} occupation. For the sample with x = 0.25, it has the optimal magnetic properties of M_s = 77 emu/g. In a SrM unit cell (a total of 24 Fe^{3+}), there are 12 Fe^{3+} occupying 12k site (spin-up), 2 Fe^{3+} occupying 2a site (spin-up), 2 Fe^{3+} occupying 2b site (spin-up), 4 Fe^{3+} occupying $4f_1$ site (spin-down) and 4 Fe^{3+} occupying $4f_2$ site (spin-down), respectively. The saturated magnetic moment of unsubstituted SrM is 40 μ_B in a unit cell, and Zn^{2+} with x = 0.25 and Sn^{4+} with x = 0.25 occupy $4f_1$ and $4f_2$ site, respectively. As a result, the magnetic moments of both tetrahedra ($4f_1$ site) and octahedra ($4f_2$ site) will vary from 20 μ_B to 17.5 μ_B, thus the saturated magnetic moment of the sample is increased to 45 μ_B, which is 12.5% higher than that of the unsubstituted SrM [38,39]. In this work, the M_s of the unsubstituted SrM is 72 emu/g, but the sample with x = 0.25 is only 6.9% higher than the SrM.
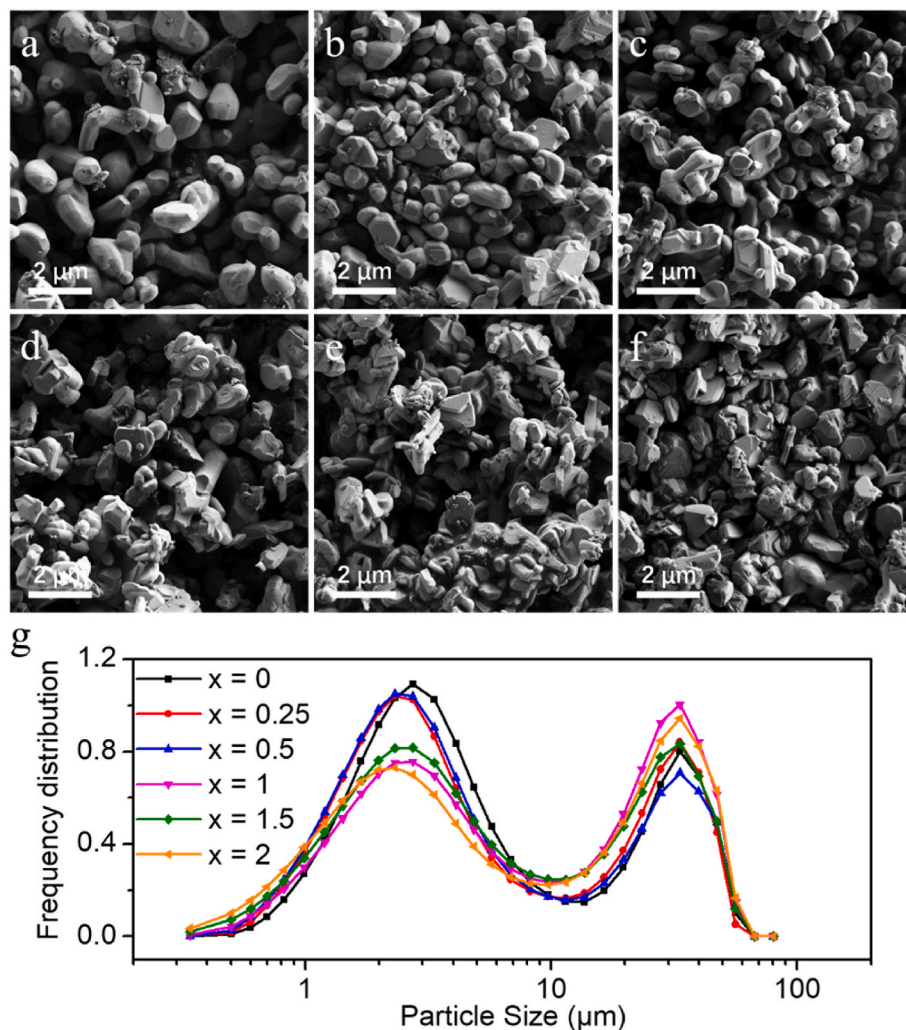

Fig. 5. Scanning electron microscopy images of the $SrFe_{12-2x}Zn_xSn_xO_{19}$: (a) x = 0, (b) 0.25, (c) 0.5, (d) 1, (e) 1.5, (f) 2. (g) The particle size distribution of $SrFe_{12-2x}Zn_xSn_xO_{19}$.

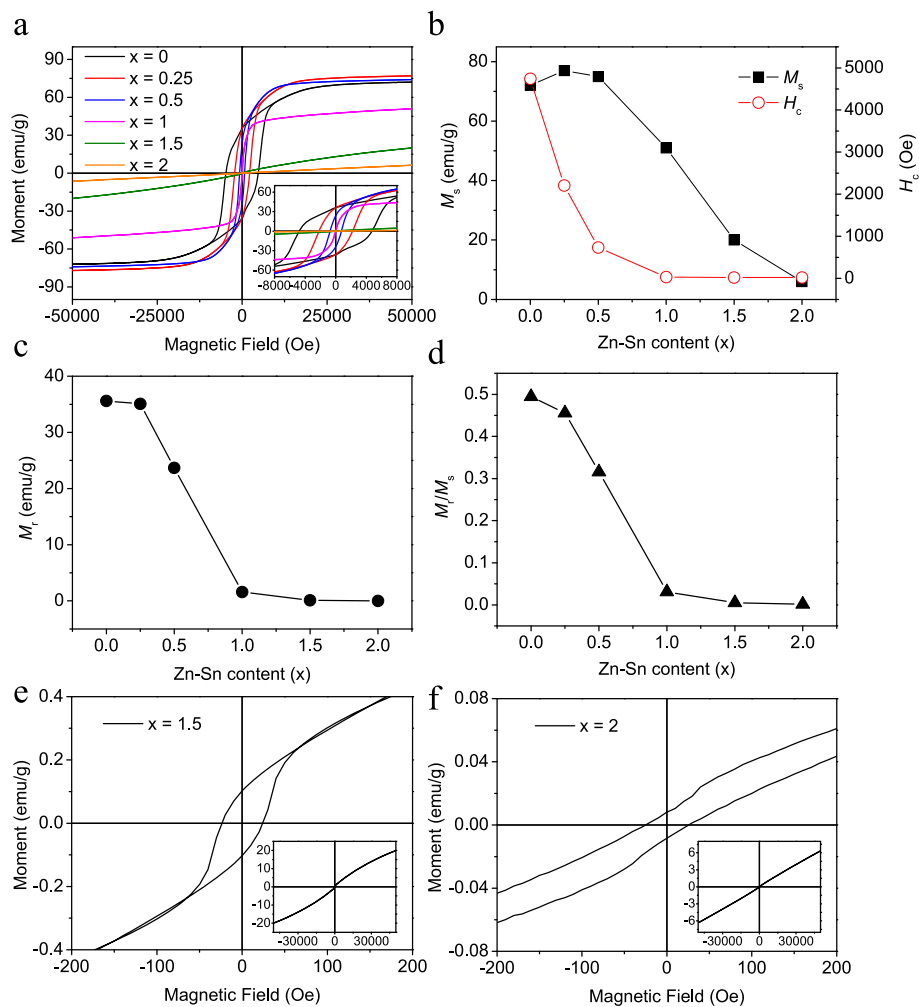**Fig. 6.** (a) Hysteresis loops and (b) the variations of M_s, H_c, (c) M_r and (d) M_r/M_s for the $SrFe_{12-2x}Zn_xSn_xO_{19}$ ($x = 0, 0.25, 0.5, 1, 1.5, 2$). The enlargement of Hysteresis loops for the sample with (e) $x = 1.5$ and (f) $x = 2$.

Reviewing the literature, it can be found that the results of theoretical simulation show that Zn^{2+} and Sn^{4+} occupy $4f_1$ and $4f_2$ sites with high probability (82%), but not 100% [39]. In SrM, only the spin direction at $4f_1$ site and $4f_2$ site is downward, while the spin direction at the other sites ($2a$, $2b$ and $12k$ sites) is upward. Namely, 18% Zn^{2+} and Sn^{4+} at the spin-down sites are required to offset the adverse effects on saturation magnetic moment caused by 18% Zn^{2+} and Sn^{4+} at the spin-up sites. Hence, the remaining 64% Zn^{2+} and Sn^{4+} at the spin-down sites can enhance the saturated magnetic moment of the sample by about 8%, corresponding well to the experimental results.

When the amount of Zn^{2+}-Sn^{4+} co-substitution is greater than or equal to 0.5, the M_s will decrease monotonously, which is due to the appearance of canted spin structure. It is known that the magnetic properties of SrM originate from the collinear arrangement of Fe^{3+} at different sites by superexchange interaction, and all the exchange interactions are antiferromagnetic [43,57]. Zn^{2+}-Sn^{4+} co-substitution has a positive effect on the M_s when the substitution amount is relatively small ($x \leq 0.25$). However, the antiferromagnetic exchange interactions between the spin-up sites and the spin-down sites are pronouncedly weakened when the amount of Zn^{2+}-Sn^{4+} co-substitution is further increased ($x \geq 0.5$). The Fe^{3+} between the spin-up sites and the Fe^{3+} between spin-down sites gradually change to antiferromagnetic arrangement (they are aligned parallel in the unsubstituted SrM). It can be found that the sample with $x = 1.5$ is canted-ferrimagnetic (Fig. 6e), while the sample with $x = 2$ is close to antiferromagnetic (Fig. 6f). The overall magnetic structure evolution process is similar to that of soft

magnetic ferrites $Zn_xFe_{3-x}O_4$ [58,59]. As shown in Fig. 6c and d, both remanence (M_r) and squareness ratio (M_r/M_s) decrease with increasing Zn^{2+}-Sn^{4+} co-substitution amount. The value of M_r/M_s is closely related to the magnetic domain structure of the particles. When the M_r/M_s is around 0.5, the particles are single domain, while the M_r/M_s is significantly lower than 0.5, the particles are multi-domain [60]. Accordingly, when the amount of Zn^{2+} - Sn^{4+} co-substitution is greater than or equal to 0.5, the samples should be multi-domain.

As can be seen in Fig. 6b, the H_c decreases rapidly with increasing Zn^{2+}-Sn^{4+} co-substitution. H_c decreases from 4742 Oe for $x = 0$ to 2206 Oe for $x = 0.25$, then rapidly decreased to 32 Oe for $x = 1$, and finally reached 22 Oe for $x = 2$. The decrease of H_c is mainly caused by three reasons: a) The magnetocrystalline anisotropy of SrM originates from strong superexchange interactions between Fe^{3+} at different sites, and the superexchange interaction is closely related to the distance of the Fe^{3+}-O^{2-} [61]. Lattice expansion increases the distance of the Fe^{3+}-O^{2-}, thus weakening the superexchange interaction between them. b) The Fe^{3+} at different five sites have different contributions to magnetocrystalline anisotropy. For the $2b$ site, $4f_2$ site, $2a$ site, $4f_1$ site, and $12k$ site, the contribution of the Fe^{3+} on the anisotropy constant K_1 is 1.4, 0.51, 0.23, 0.18, and -0.18, respectively [5]. Among these, the $4f_1$ sites and $4f_2$ sites have a positive effect on the magnetocrystalline anisotropy, so that the occupation of the $4f_1$ sites and $4f_2$ sites by nonmagnetic Zn^{2+} and Sn^{4+} leads to a decrease on magnetocrystalline anisotropy, which in turn is reflected in a decrease on H_c. c) With increasing Zn^{2+} - Sn^{4+} co-substitution, the magnetic domain structure of the samples

change from single domain to multi-domain ($x \geq 0.5$). The magnetization mechanism changes from the rotation of magnetization to the easy movement of the domain walls, which causes a decrease on H_c [62,63].

4. Conclusion

In this paper, the effect of Zn^{2+}-Sn^{4+} co-substitution on structure and magnetic properties of SrM was investigated. With increasing Zn^{2+}-Sn^{4+} co-substitution, the samples exhibit obvious lattice expansion, which is mainly due to the fact that the ionic radii of Zn^{2+} and Sn^{4+} are larger than those of Fe^{3+}. In terms of magnetic properties, the M_s of powder samples reaches the maximum value $M_s = 77$ emu/g at $x = 0.25$, which is attributed to the Zn^{2+} and Sn^{4+} occupy the spin-down $4f_1$ and $4f_2$ sites, respectively. When the amount of Zn^{2+}-Sn^{4+} co-substitution is greater than or equal to 0.5, the M_s and H_c of the sample will decrease monotonically, which is closely related to the nonmagnetic ions weakening the superexchange interaction. Overall, Zn^{2+}-Sn^{4+} co-substitution can effectively enhance the M_s and reduce the H_c, this material ($x = 0.25$) is expected to be a candidate material for high-density magnetic recording, just like Co^{2+}-Ti^{4+} co-substituted BaM and SrM.

Credit author statement

Xiang Yu: Conceptualization, Methodology, Investigation, Writing - original draft. **Ningfang Zhou:** Validation, Writing - review & editing. **Ruoshui Liu:** Data curation. **Lichen Wang:** Formal analysis. **Zhiyi Xu:** Software. **Huayang Gong:** Supervision, Resources. **Tongyun Zhao:** Funding acquisition, Project administration. **Jirong Sun:** Funding acquisition. **Fengxia Hu:** Funding acquisition. **Baogen Shen:** Writing - review & editing, Supervision, Funding acquisition.

Declaration of competing interest

The authors declare that they have no known competing financial interests or personal relationships that could have appeared to influence the work reported in this paper.

Data availability

The authors do not have permission to share data.

Acknowledgments

References

[1] U. Topal, H.I. Bakan, Magnetic properties and remanence analysis in permanently magnetic $BaFe_{12}O_{19}$ foams, J. Eur. Ceram. Soc. 30 (2010) 3167–3171.

[2] B. Abraime, M. Ait Tamerd, A. Mahmoud, F. Boschini, A. Benyoussef, M. Hamedoun, Y. Xiao, A. El Kenz, O. Mounkachi, Experimental and theoretical investigation of $SrFe_{12}O_{19}$ nanopowder for permanent magnet application, Ceram. Int. 43 (2017) 15999–16006.

[3] J.C. Guzmán-Mínguez, V. Fuertes, C. Granados-Miralles, J.F. Fernández, A. Quesada, Greener processing of $SrFe_{12}O_{19}$ ceramic permanent magnets by two-step sintering, Ceram. Int. 47 (2021) 31765–31771.

[4] Y. Yang, F. Wang, J. Shao, D. Huang, H. He, A.V. Trukhanov, S.V. Trukhanov, Influence of Nd-NbZn co-substitution on structural, spectral and magnetic properties of M-type calcium-strontium hexaferrites $Ca_{0.4}Sr_{0.6-x}Nd_xFe_{12.0-x}(Nb_{0.5}Zn_{0.5})_xO_{19}$, J. Alloys Compd. 765 (2018) 616–623.

[5] J. Li, H. Zhang, Y. Liu, Q. Li, T. Zhou, H. Yang, Phase formation, magnetic properties and Raman spectra of Co–Ti co-substitution M-type barium ferrites, Appl. Phys. A 119 (2015) 525–532.

[6] I. Ali, M.U. Islam, M.S. Awan, M. Ahmad, Effects of Ga–Cr substitution on structural and magnetic properties of hexaferrite ($BaFe_{12}O_{19}$) synthesized by sol–gel auto-combustion route, J. Alloys Compd. 547 (2013) 118–125.

[7] S.V. Trukhanov, A.V. Trukhanov, V.G. Kostishin, L.V. Panina, I.S. Kazakevich, V.A. Turchenko, V.V. Oleinik, E.S. Yakovenko, L.Y. Matsui, Magnetic and absorbing properties of M-type substituted hexaferrites $BaFe_{12-x}Ga_xO_{19}$ (0.1 < x < 1.2), J. Exp. Theor. Phys. 123 (2016) 461–469.

[8] S.V. Trukhanov, A.V. Trukhanov, M.M. Salem, E.L. Trukhanova, L.V. Panina, V.G. Kostishyn, M.A. Darwish, A.V. Trukhanov, T.I. Zubar, D.I. Tishkevich, V. Sivakov, D.A. Vinnik, S.A. Gudkova, C. Singh, Preparation and investigation of structure, magnetic and dielectric properties of $(BaFe_{11.9}Al_{0.1}O_{19})_{1-x}$ - $(BaTiO_3)_x$ bicomponent ceramics, Ceram. Int. 44 (2018) 21295–21302.

[9] D.S. Klygach, M.G. Vakhitov, D.A. Vinnik, A.V. Bezborodov, S.A. Gudkova, V.E. Zhivulin, D.A. Zherebtsov, C.P. SakthiDharan, S.V. Trukhanov, A.V. Trukhanov, A.Y. Starikov, Measurement of permittivity and permeability of barium hexaferrite, J. Magn. Magn Mater. 465 (2018) 290–294.

[10] A.V. Trukhanov, V.G. Kostishyn, L.V. Panina, V.V. Korovushkin, V.A. Turchenko, P. Thakur, A. Thakur, Y. Yang, D.A. Vinnik, E.S. Yakovenko, L.Y. Matzui, E.L. Trukhanova, S.V. Trukhanov, Control of electromagnetic properties in substituted M-type hexagonal ferrites, J. Alloys Compd. 754 (2018) 247–256.

[11] D.A. Vinnik, D.S. Klygach, V.E. Zhivulin, A.I. Malkin, M.G. Vakhitov, S.A. Gudkova, D.M. Galimov, D.A. Zherebtsov, E.A. Trofimov, N.S. Knyazev, V.V. Atuchin, S.V. Trukhanov, A.V. Trukhanov, Electromagnetic properties of $BaFe_{12}O_{19}$:Ti at centimeter wavelengths, J. Alloys Compd. 755 (2018) 177–183.

[12] H. Kaur, A. Marwaha, C. Singh, S.B. Narang, R. Jotania, S. Jacobo, A.S.B. Sombra, S.V. Trukhanov, A.V. Trukhanov, P. Dhruv, Investigation of structural, hysteresis and electromagnetic parameters for microwave absorption application in doped Ba–Sr hexagonal ferrites at X-band, J. Alloys Compd. 806 (2019) 1220–1229.

[13] S.V. Trukhanov, A.V. Trukhanov, V.A. Turchenko, A.V. Trukhanov, E.L. Trukhanova, D.I. Tishkevich, V.M. Ivanov, T.I. Zubar, M. Salem, V.G. Kostishyn, L.V. Panina, D.A. Vinnik, S.A. Gudkova, Polarization origin and iron positions in indium doped barium hexaferrites, Ceram. Int. 44 (2018) 290–300.

[14] A.V. Trukhanov, V.A. Turchenko, V.G. Kostishin, F. Damay, F. Porcher, N. Lupu, B. Bozzo, I. Fina, S. Polosan, M.V. Silibin, M.M. Salem, D.I. Tishkevich, S.V. Trukhanov, The origin of the dual ferroic properties in quasi-centrosymmetrical $SrFe_{12-x}In_xO_{19}$ hexaferrites, J. Alloys Compd. 886 (2021), 161249.

[15] V. Turchenko, V.G. Kostishyn, S. Trukhanov, F. Damay, F. Porcher, M. Balasoiu, N. Lupu, B. Bozzo, I. Fina, A. Trukhanov, J. Waliszewski, K. Recko, S. Polosan, Crystal and magnetic structures, magnetic and ferroelectric properties of strontium ferrite partially substituted with ions, J. Alloys Compd. 821 (2020) 153412.

[16] R.C. Pullar, Hexagonal ferrites: a review of the synthesis, properties and applications of hexaferrite ceramics, Prog. Mater. Sci. 57 (2012) 1191–1334.

[17] C. de Julián Fernández, C. Sangregorio, J. de la Figuera, B. Belec, D. Makovec, A. Quesada, Progress and prospects of hard hexaferrites for permanent magnet applications, J. Phys. D Appl. Phys. 54 (2021) 153001.

[18] D.A. Vinnik, V.E. Zhivulin, D.A. Uchaev, S.A. Gudkova, D.E. Zhivulin, A.Y. Starikov, S.V. Trukhanov, V.A. Turchenko, T.I. Zubar, T.P. Gavrilova, R.M. Eremina, E. Fadeev, E. Lähderanta, A.S.B. Sombra, D. Zhou, R.B. Jotania, C. Singh, A.V. Trukhanov, Effect of titanium substitution and temperature variation on structure and magnetic state of barium hexaferrites, J. Alloys Compd. 859 (2021), 158365.

[19] A.V. Trukhanov, K.A. Darwish, M.M. Salem, O.M. Hemeda, M.I. Abdel Ati, M.A. Darwish, E.Y. Kaniukov, S.V. Podgornaya, V.A. Turchenko, D.I. Tishkevich, T.I. Zubar, K.A. Astapovich, V.G. Kostishyn, S.V. Trukhanov, Impact of the heat treatment conditions on crystal structure, morphology and magnetic properties evolution in BaM nanohexaferrites, J. Alloys Compd. 866 (2021), 158961.

[20] S. Dong, C. Lin, X. Meng, One-pot synthesis and microwave absorbing properties of ultrathin $SrFe_{12}O_{19}$ nanosheets, J. Alloys Compd. 783 (2019) 779–784.

[21] T.P. Poudel, D. Guragain, J. Mohapatra, J.P. Liu, S.R. Mishra, Novel molten salt assisted autocombustion method for the synthesis of aluminum-doped $SrFe_{12-x}Al_xO_{19}$ hexaferrite nanoparticles, J. Nanosci. Nanotechnol. 20 (2020) 7735–7742.

[22] M. Kim, K. Lee, M. Choi, J. Kim, Magnetic properties and morphologies of synthesized strontium ferrite powders by the molten salt method, IEEE Trans. Magn. 54 (2018) 1–4.

[23] P. Maltoni, T. Sarkar, G. Barucca, G. Varvaro, F. Locardi, D. Peddis, R. Mathieu, Tuning the magnetic properties of hard–soft $SrFe_{12}O_{19}/CoFe_2O_4$ nanostructures via composition/interphase coupling, J. Phys. Chem. C 125 (2021) 5927–5936.

[24] A. Alipour, S. Torkian, A. Ghasemi, M. Tavoosi, G.R. Gordani, Magnetic properties improvement through exchange-coupling in hard/soft $SrFe_{12}O_{19}/Co$ nanocomposite, Ceram. Int. 47 (2021) 2463–2470.

[25] R. Liu, D.a. Wu, X. Yu, N. Zhou, D. Liu, L. Wang, Z. Xu, H. Gong, T. Zhao, J. Sun, F. Hu, B. Shen, Improved magnetic properties of self-composite $SrFe_{12}O_{19}$ powder prepared by Fe_3O_4 nanoparticles, Arab. J. Chem. 15 (2022), 104071.

[26] R. Sun, X. Li, A. Xia, S. Su, C. Jin, Hexagonal $SrFe_{12}O_{19}$ ferrite with high saturation magnetization, Ceram. Int. 44 (2018) 13551–13555.

[27] M.A.P. Buzinaro, N.S. Ferreira, F. Cunha, M.A. Macêdo, Hopkinson effect, structural and magnetic properties of M-type Sm^{3+}-doped $SrFe_{12}O_{19}$ nanoparticles produced by a proteic sol–gel process, Ceram. Int. 42 (2016) 5865–5872.

[28] C. Liu, X. Kan, S. Liu, S. Feng, J. Hu, W. Wang, K.M. Ur Rehman, M. Shezad, Influence of the Eu substitution on the structure and magnetic properties of the Sr-hexaferrites, Ceram. Int. 46 (2020) 171–179.

[29] J. Hu, C. Liu, X. Kan, X. Liu, S. Feng, Q. Lv, Y. Yang, W. Wang, M. Shezad, K.M. Ur Rehman, Structure and magnetic performance of Gd substituted Sr-based hexaferrites, J. Alloys Compd. 820 (2020), 153180.

[30] X. Liu, P. Hernández-Gómez, K. Huang, S. Zhou, Y. Wang, X. Cai, H. Sun, B. Ma, Research on La^{3+}-Co^{2+}-substituted strontium ferrite magnets for high intrinsic coercive force, J. Magn. Magn Mater. 305 (2006) 524–528.

[31] N. Yasmin, S. Abdulsatar, M. Hashim, M. Zahid, S. Fatima Gillani, A. Kalsoom, M. Naeem Ashiq, I. Inam, M. Safdar, M. Mirza, Structural and magnetic studies of Ce-Mn doped M-type SrFe$_{12}$O$_{19}$ hexagonal ferrites by sol-gel auto-combustion method, J. Magn. Magn Mater. 473 (2019) 464–469.

[32] Y. Yang, J. Shao, F. Wang, D. Huang, Z. Wu, Synthesis, crystal structure and magnetic characterization of Pr^{3+} and Zn^{2+} ions co-doped hexagonal ferrites via the ceramic process, Chinese J. Phys. 56 (2018) 2075–2084.

[33] A.V. Trukhanov, M.A. Darwish, L.V. Panina, A.T. Morchenko, V.G. Kostishyn, V. A. Turchenko, D.A. Vinnik, E.L. Trukhanova, K.A. Astapovich, A.L. Kozlovskiy, M. Zdorovets, S.V. Trukhanov, Features of crystal and magnetic structure of the BaFe$_{12-x}$Ga$_x$O$_{19}$ (x $\leq$ 2) in the wide temperature range, J. Alloys Compd. 791 (2019) 522–529.

[34] C. Liu, X. Kan, F. Hu, X. Liu, S. Feng, J. Hu, W. Wang, K.M. Ur Rehman, M. Shezad, C. Zhang, H. Li, S. Zhou, Q. Wu, Characterizations of magnetic transition behavior and electromagnetic properties of Co-Ti co-substituted SrM-based hexaferrites SrCo$_x$Ti$_x$Fe$_{12-2x}$O$_{19}$ compounds, J. Alloys Compd. 784 (2019) 1175–1186.

[35] M.N. Ashiq, M.J. Iqbal, I.H. Gul, Structural, magnetic and dielectric properties of Zr–Cd substituted strontium hexaferrite (SrFe$_{12}$O$_{19}$) nanoparticles, J. Alloys Compd. 487 (2009) 341–345.

[36] S. Zhang, C. Meng, L. Zhang, S. Yuan, H. Luo, S. Liu, H. Chang, Effect of Zn and Ir doping on microwave absorption of SrFe$_{12-2x}$Zn$_x$Ir$_x$O$_{19}$, J. Magn. Magn Mater. 513 (2020), 167076.

[37] Y.H. Hou, X. Chen, X.L. Guo, W. Li, Y.L. Huang, X.M. Tao, Effects of intrinsic defects and doping on SrFe$_{12}$O$_{19}$: a first-principles exploration of the structural, electronic and magnetic properties, J. Magn. Magn Mater. 538 (2021), 168257.

[38] L.S.I. Liyanage, S. Kim, Y.-K. Hong, J.-H. Park, S.C. Erwin, S.-G. Kim, Theory of magnetic enhancement in strontium hexaferrite through Zn–Sn pair substitution, J. Magn. Magn Mater. 348 (2013) 75–81.

[39] V. Dixit, D. Thapa, B. Lamichhane, C.N. Nandadasa, Y.-K. Hong, S.-G. Kim, Site preference and magnetic properties of Zn-Sn-substituted strontium hexaferrite, J. Appl. Phys. 125 (2019), 173901.

[40] A.V. Trukhanov, V.O. Turchenko, I.A. Bobrikov, S.V. Trukhanov, I.S. Kazakevich, A.M. Balagurov, Crystal structure and magnetic properties of the BaFe$_{12-x}$Al$_x$O$_{19}$ (x=0.1–1.2) solid solutions, J. Magn. Magn Mater. 393 (2015) 253–259.

[41] S.V. Trukhanov, A.V. Trukhanov, V.A. Turchenko, V.G. Kostishyn, L.V. Panina, I. S. Kazakevich, A.M. Balagurov, Structure and magnetic properties of BaFe$_{11.9}$In$_{0.1}$O$_{19}$ hexaferrite in a wide temperature range, J. Alloys Compd. 689 (2016) 383–393.

[42] A.V. Trukhanov, K.A. Astapovich, M.A. Almessiere, V.A. Turchenko, E. L. Trukhanova, V.V. Korovushkin, A.A. Amirov, M.A. Darwish, D.V. Karpinsky, D. A. Vinnik, D.S. Klygach, M.G. Vakhitov, M.V. Zdorovets, A.L. Kozlovskiy, S. V. Trukhanov, Pecularities of the magnetic structure and microwave properties in Ba(Fe$_{1-x}$Sc$_x$)$_{12}$O$_{19}$ (x<0.1) hexaferrites, J. Alloys Compd. 822 (2020), 153575.

[43] J. Bai, X. Liu, T. Xie, F. Wei, Z. Yang, The effects of La–Zn substitution on the magnetic properties of Sr-magnetoplumbite ferrite nano-particles, Mater. Sci. Eng., B 68 (2000) 182–185.

[44] M.A. Almessiere, Y. Slimani, A. Baykal, Impact of Nd-Zn co-substitution on microstructure and magnetic properties of SrFe$_{12}$O$_{19}$ nanohexaferrite, Ceram. Int. 45 (2019) 963–969.

[45] R.D. Shannon, Revised effective ionic radii and systematic studies of interatomic distances in halides and chalcogenides, Acta Cryst. A 32 (1976) 751–767.

[46] T.R. Wagner, Preparation and crystal structure analysis of magnetoplumbite-type BaGa$_{12}$O$_{19}$, J. Solid State Chem. 136 (1998) 120–124.

[47] V. Rathod, A.V. Anupama, R.V. Kumar, V.M. Jali, B. Sahoo, Correlated vibrations of the tetrahedral and octahedral complexes and splitting of the absorption bands in FTIR spectra of Li-Zn ferrites, Vib. Spectrosc. 92 (2017) 267–272.

[48] R.S. Alam, M. Moradi, M. Rostami, H. Nikmanesh, R. Moayedi, Y. Bai, Structural, magnetic and microwave absorption properties of doped Ba-hexaferrite nanoparticles synthesized by co-precipitation method, J. Magn. Magn Mater. 381 (2015) 1–9.

[49] S. Shooshtary Veisi, M. Yousefi, M.M. Amini, A.R. Shakeri, M. Bagherzadeh, Magnetic and microwave absorption properties of Cu/Zr doped M-type Ba/Sr hexaferrites prepared via sol-gel auto-combustion method, J. Alloys Compd. 773 (2019) 1187–1194.

[50] T. Xie, L. Xu, C. Liu, Y. Wang, Magnetic composite ZnFe$_2$O$_4$/SrFe$_{12}$O$_{19}$: preparation, characterization, and photocatalytic activity under visible light, Appl. Surf. Sci. 273 (2013) 684–691.

[51] A. Shokri, S.F. Shayesteh, K. Boustani, The role of Co ion substitution in SnFe$_2$O$_4$ spinel ferrite nanoparticles: study of structural, vibrational, magnetic and optical properties, Ceram. Int. 44 (2018) 22092–22101.

[52] J. Kreisel, G. Lucazeau, H. Vincent, Raman spectra and vibrational analysis of BaFe$_{12}$O$_{19}$ hexagonal ferrite, J. Solid State Chem. 137 (1998) 127–137.

[53] H.H. Nguyen, W.H. Jeong, T.L. Phan, B.W. Lee, D.S. Yang, N. Tran, N.T. Dang, Coexistence of Zn and Fe ions influenced magnetic and microwave shielding properties of Zn-doped SrFe$_{12}$O$_{19}$ ferrites, J. Magn. Magn Mater. 537 (2021), 168195.

[54] M.A.P. Buzinaro, M.A. Macêdo, B.F.O. Costa, N.S. Ferreira, Disorder of Fe$^{(2)}$O$_5$ bipyramids and spin-phonon coupling in SrFe$_{12}$O$_{19}$ nanoparticles, Ceram. Int. 45 (2019) 13571–13574.

[55] J. Kreisel, G. Lucazeau, H. Vincent, Raman study of substituted barium ferrite single crystals, BaFe$_{12-2x}$Me$_x$Co$_x$O19 (Me=Ir, Ti), J. Raman Spectrosc. 30 (1999) 115–120.

[56] M. Zhang, Q. Liu, G. Zhu, S. Xu, Magnetic properties of Co and Ti co-doped strontium hexaferrite prepared by sol–gel method, Appl. Phys. A 125 (2019) 191.

[57] A. Isalgué, A. Labarta, J. Tejada, X. Obradors, Exchange interactions in BaFe$_{12}$O$_{19}$, Appl. Phys. A 39 (1986) 221–225.

[58] Y. Yafet, C. Kittel, Antiferromagnetic arrangements in ferrites, Phys. Rev. 87 (1952) 290–294.

[59] N. Modaresi, R. Afzalzadeh, B. Aslibeiki, P. Kameli, A. Ghotbi Varzaneh, I. Orue, V. A. Chernenko, Magnetic properties of Zn$_x$Fe$_{3-x}$O$_4$ nanoparticles: a competition between the effects of size and Zn doping level, J. Magn. Magn Mater. 482 (2019) 206–218.

[60] C.C. Chauhan, A.R. Kagdi, R.B. Jotania, A. Upadhyay, C.S. Sandhu, S.E. Shirsath, S. S. Meena, Structural, magnetic and dielectric properties of Co-Zr substituted M-type calcium hexagonal ferrite nanoparticles in the presence of α-Fe$_2$O$_3$ phase, Ceram. Int. 44 (2018) 17812–17823.

[61] M.A. Gilleo, Superexchange interaction energy for Fe^{3+}-O^{2-}-Fe^{3+} linkages, Phys. Rev. 109 (1958) 777–781.

[62] N. Kumar, A. Kumar, R. Jha, A. Dogra, R. Pasricha, R.K. Kotnala, H. Kishan, V.P. S. Awana, Impact of particle size on room temperature ferrimagnetism of SrFe$_{12}$O$_{19}$, J. Supercond. Nov. Magn. 23 (2010) 423–427.

[63] Z.F. Zi, Y.P. Sun, X.B. Zhu, Z.R. Yang, J.M. dai, W.H. Song, Structural and magnetic properties of SrFe$_{12}$O$_{19}$ hexaferrite synthesized by a modified chemical co-precipitation method, J. Magn. Magn Mater. 320 (2008) 2746–2751.